Journal of Thermal Analysis and Calorimetry
https://doi.org/10.1007/s10973-024-13584-9

Exploring the potentialities of thermal asymmetries in composite wind turbine blade structures via numerical and thermographic methods: a thermophysical perspective

A. A. A. Figueiredo[1,2] · G. D'Alessandro[3] · S. Perilli[4] · S. Sfarra[3] · H. Fernandes[5,6]

Received: 22 March 2024 / Accepted: 12 August 2024
© The Author(s) 2024

Abstract
Using composite materials in turbine blades has become common in the wind power industry due to their mechanical properties and low mass. This work aims to investigate the effectiveness of the active infrared thermography technique as a non-destructive inspection tool to identify defects in composite material structures of turbine blades. Experiments were carried out by heating the sample and capturing thermographic images using a thermal camera in four different scenarios, changing the heating strategy. Such a preliminary experiments are prodromic to build, in future, the so-called optimal experiment design for thermal property estimation. The experimental results using two heaters arranged symmetrically on the sample detected the presence of the defect through temperature curves extracted from thermal images, where temperature asymmetries of 25% between the regions with and without defect occurred. Moreover, when only a larger heater was used in transmission mode, the defect was detected based on differences between normalized excess temperatures on the side with and without the defect in the order of 20%. Additionally, numerical simulations were carried out to present solutions for improving defect detection. It was demonstrated that active infrared thermography is an efficient technique for detecting flaws in composite material structures of turbine blades. This research contributes to advancing knowledge in inspecting composite materials.

Keywords Composite · Turbine blades · Defect · Thermography · Thermophysical properties · Heat transfer

Introduction

The blades of wind turbines are critical components and susceptible to various damages during their operation, which can affect other blades and turbines, increasing the costs of the energy generation process. The blades consist of two fiberglass composite halves held together by shear webs and strong adhesives. The composite structures of the blades can present different types of damage, such as delamination, cracks, air pockets, and fiber-matrix detachments. Adverse environmental conditions can also cause damage. The use of non-destructive testing (NDT) to monitor the conditions of the blades is essential for the early detection of failures [1].

✉ H. Fernandes
h.fernandes@cranfield.ac.uk

A. A. A. Figueiredo
alissonfigueiredo@professor.uema.br

G. D'Alessandro
giampaolo.dalessandro@univaq.it

S. Perilli
stefano.perilli@uniroma1.it

S. Sfarra
stefano.sfarra@univaq.it

[1] Department of Mechanical Engineering, State University of Maranhao, São Luís, Brazil

[2] Post-Graduate Program in Mechanical Engineering, Federal Institute of Maranhao, São Luís, Brazil

[3] Department of Industrial and Information Engineering and Economics, University of L'Aquila, L'Aquila, Italy

[4] Department of Information Engineering, Electronics and Telecommunications, Sapienza University of Rome, Rome, Italy

[5] IVHM Centre, Faculty of Engineering and Applied Sciences, Cranfield University, Cranfield, UK

[6] Faculty of Computing, Federal University of Uberlandia, Uberlandia, Brazil

Published online: 16 September 2024

In recent years, several traditional and innovative NDTs have emerged for both areas of application. These techniques encompass methods that include visual inspection, strain measurement, acoustic emission, ultrasound, vibration, thermography, machine vision, and many other. NDTs can be carried out by a human team, using robots or using unmanned aerial vehicles [2]. Furthermore, these techniques can be employed both in individual wind turbines and systematically in onshore or offshore wind farms. Non-destructive approaches were extensively reviewed and discussed, and possible research directions were highlighted [3–5].

Infrared thermography is an NDT technique that detects internal defects in materials qualitatively and quantitatively without physical contact. The technique was developed to accurately predict the depth of defects and has successfully been applied in several areas. Infrared thermography offers a comprehensive approach to defect detection, allowing for large-area analysis and providing valuable information about the integrity of materials. Infrared thermography helps in decision-making for maintenance and quality control [7].

Localized heating can introduce significant challenges in interpreting the images obtained. Several works have studied the two-dimensionality of the heat flow, which makes the analysis of thermal images difficult, as the heat diffuses not only along the thickness axis of the material, but also laterally, amplifying the blurring effect [8–10].

Different studies have used infrared thermography to detect faults in wind turbine blades. To the best of our knowledge, the first one can be attributed to A.P. Pontello, who in 1974 applied infrared thermography on turbine blades containing flaws covered by corrosion [12]. Passive and active thermography have been used to monitor the condition of these types of defects [1]. Passive infrared thermography was used to detect internal defects and evaluate the thermal behavior of structures in different climatic conditions [13, 14]. Active thermography has been applied to qualitatively and quantitatively evaluate the presence of defects in turbine composite materials [16, 17].

Several works have carried out numerical modeling of active infrared thermography, essential for simulating defects in composites, such as cracks and delaminations [18–22]. The creation of models that accurately characterize the thermal and structural behavior of composite materials under different test conditions makes it possible to predict the thermal response of internal defects when subjected to thermal stimuli, contributing to the development of more efficient non-destructive inspection techniques.

Studies have been developed using different types of excitations to inspect samples of wind turbine blades with defects, including foreign materials, air inclusions, and manufacturing flaws. Optimization of algorithms and utilization of image filtering play an essential role in thermography-based failure analysis [24–27]. However, further studies need to be conducted with the aim of assessing new possibilities for enhancing methodologies for infrared thermography-based fault identification.

The main objective of this work is to investigate the effectiveness of the active infrared thermography technique as a non-destructive inspection tool to identify defects in composite material structures of turbine blades. Experiments were conducted in the laboratory to detect an artificial polyvinyl chloride (PVC) inclusion in the sample. The active approach was applied by heating the sample through thermal resistances or a heating plate installed in transmission mode. The reproduced wind turbine blade cooled down naturally. A thermographic camera recorded thermal images of the sample's surface during the heating and cooling steps. Four different scenarios were analyzed to determine the best strategies for detecting the defect. Numerical simulations using the commercial software COMSOL® were carried out to study the experimental results and predict the numerical temperature distribution starting from the correct application of the boundary conditions. Since the defect is very thin, by considering the symmetry of the heating with respect to the size of the sample, the proposed thermal stimulus can be considered of interest to provide solid conclusions on the defect detection based on slight bendings of the thermal imprints [29, 30].

This paper presents in Sect. 2 the methodology and materials used, including the mathematical modeling, experimental procedures and numerical approach used. The results are discussed in Sect. 3, where analyses of experiments and numerical simulations are performed. In conclusion, in Sect. 4, a synthesis of the main results and suggestions for future research is presented.

Materials and methods

Figure 1 shows the configuration of the experiments performed, where the sample was characterized by two glass fiber/epoxy matrix composite plates and an artificial polyvinyl chloride (PVC) inclusion was considered a defect. Figure 1a shows an overview of the experiment, highlighting the power source that powered the heaters, the timer relay to control the heating duration, and the composite sample along with its holder. Figure 1b shows the scenario where two heaters were utilized on the rear surface, while Fig. 1c shows the heater plate employed in transmission mode. Figure 1d shows a schematic configuration of the experiment. A FLIR T1020 thermal camera (1024 x 768 pixels resolution) was used to record thermal images from the front surface.

In particular, the initial Cytec 919 composite specimen consists of two layers of glass fiber oriented at 0°. During the manufacturing process, a foreign material (PVC) was inserted between the layers with the aim of simulating a

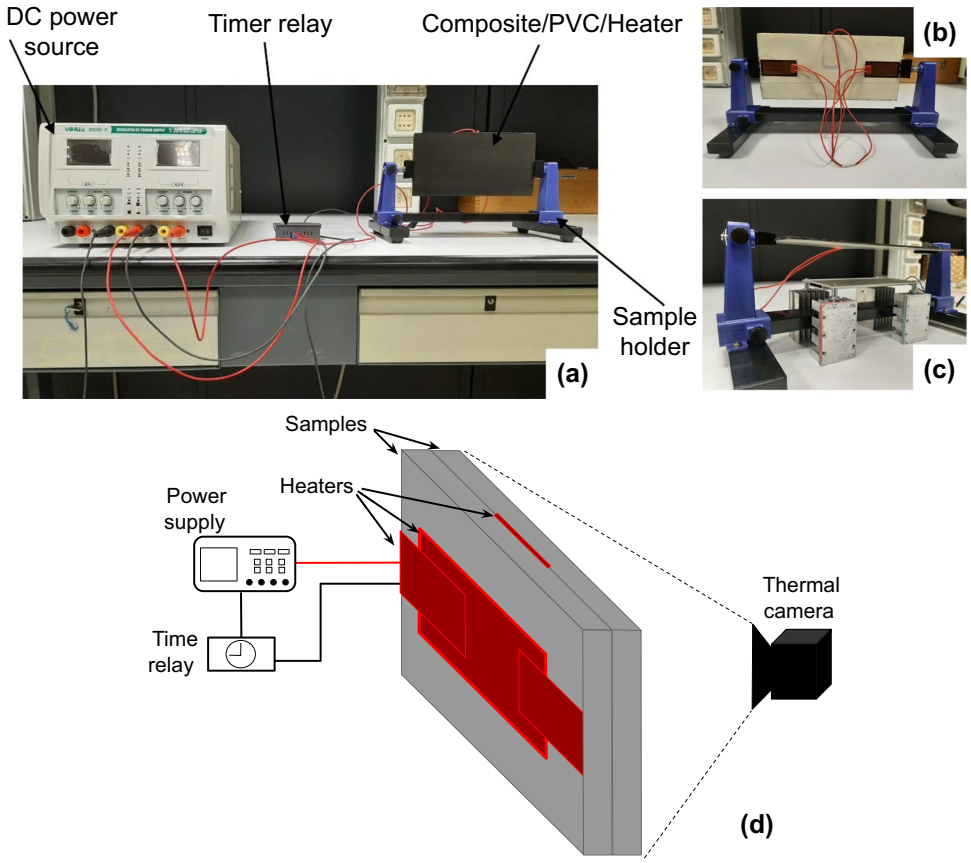


Fig. 1 Experimental setup with IR camera in the laboratory: **a** overview, **b** two heaters, **c** heater plate, and **d** schematic setup

defect (inclusion). The initial specimen (from which the final specimen described thereafter was realized) is shown in Fig. 2. To evaluate the thickness of the sample, it was decided to acquire at least 4 thicknesses in different points. Figure 3a shows the thickness measurement points within the areas marked with red circles. It is possible to see the composite slab on the rectified surface of the Fanuc brand 18i-MB gantry milling machine. The cylindrical steel mass visible in Fig. 3b has the task of keeping the entire surface of the sample in contact with the milling machine surface. It is possible to see an enlargement of the Borletti brand comparator with thousandth accuracy, in contact with the workpiece table centered at 0 to allow the Z-axis of the machine to be zeroed.

After the measurement procedure, the specimen was removed from the machine and placed on a special work

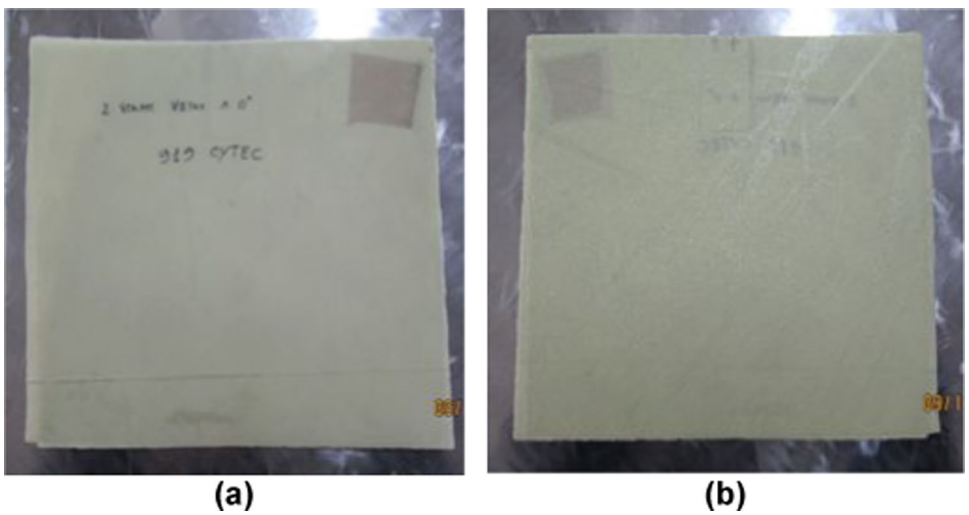


Fig. 2 Cytec 919 specimen: **a** front side of the specimen and **b** back side of the specimen

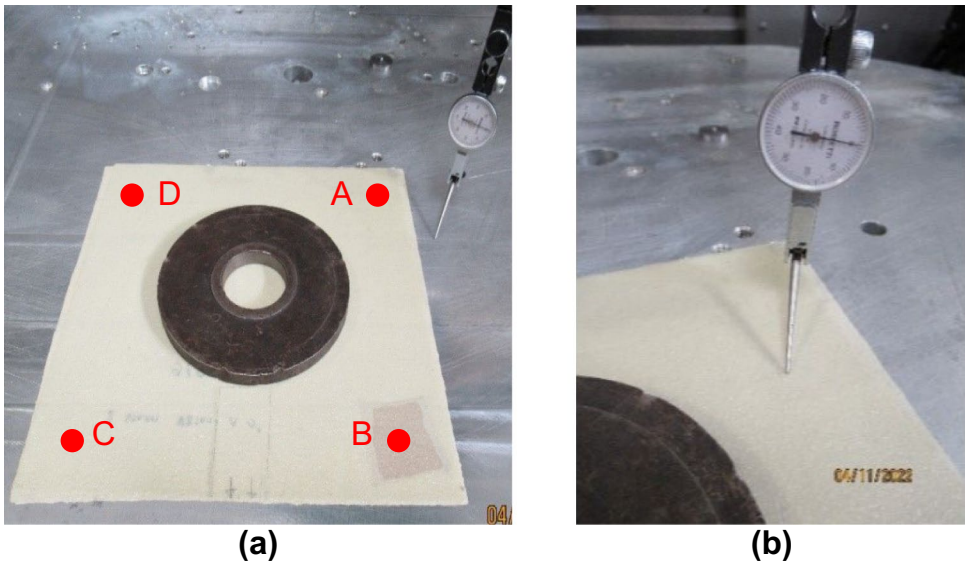


Fig. 3 Position of the composite plate on the measuring plane: **a** general view and **b** detail of the measuring probe on 0 to allow the piece zero procedure

bench where squaring and trimming are carried out until a rectangle is obtained. Then, the specimen was split into equal parts as depicted in Fig. 4a. An electrical resistance was juxtaposed on one of the surfaces of the specimen, through its adhesive layer, with the aim of generating a local thermal load. This resistance is of a commercial nature and the thickness was measured (given the regularity of the product) in a single point with the aid of a twentieth caliper. After having made the electrical resistance (i.e., the electric heater) integral to the specimen, the surfaces having a higher roughness were sprinkled with a very high-temperature resistant glue (sprayed on the surface), creating a homogeneous and regular layer. The two segments were juxtaposed, both on the surfaces covered by the glue, thus forming the final specimen shown in Fig. 4b. Figure 4c illustrates the final painted sample mounted on the sample holder.

Figure 5 shows a schematic drawing detailing the sample used in the experiments, where each composite plate has width, height measured with a common metric rod with precision in the order of mm equal to 203 and 101, respectively, while the thickness was measured with a millesimal dial comparator, and it is equal to 0.765 mm. The PVC inclusion has a thickness of 0.17 mm and is located 0.30 mm away from the front surface (surface monitored by the thermal camera). As the thickness of the inclusion inserted into the composite is very thin, this minimizes the existence of lateral flows in the thermographic images, limiting the blurring effect and thus facilitating the analysis of the results.

Four different heating scenarios were designed to apply a thermal excitation to the sample. In scenario 1, a heater covered with polyimide layers of dimensions 44.00, 19.00, and 0.10 mm was inserted between the two composite plates

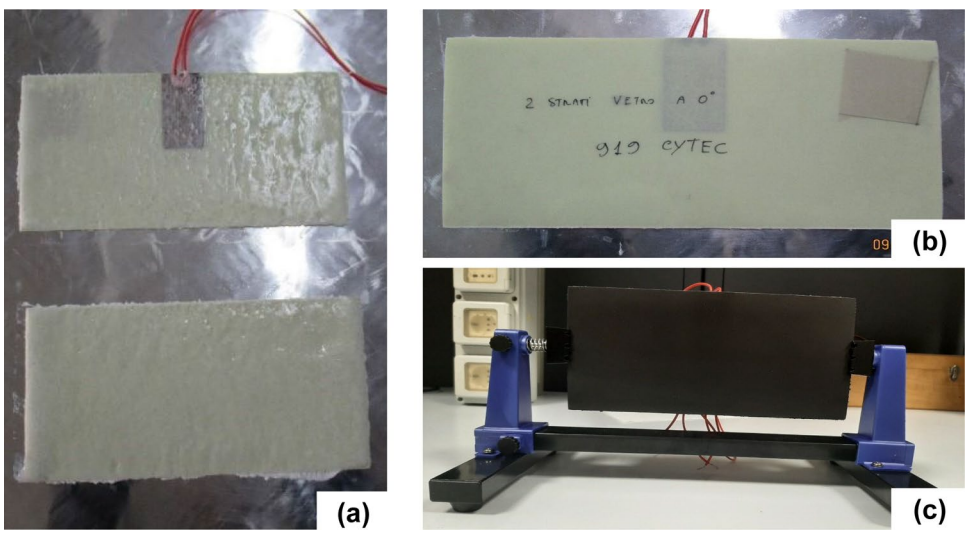


Fig. 4 Final stages of sample manufacturing: **a** adhesive deposited on sample surfaces, **b** Specimen glued with the electrical resistance present between the two pieces and **c** final painted sample

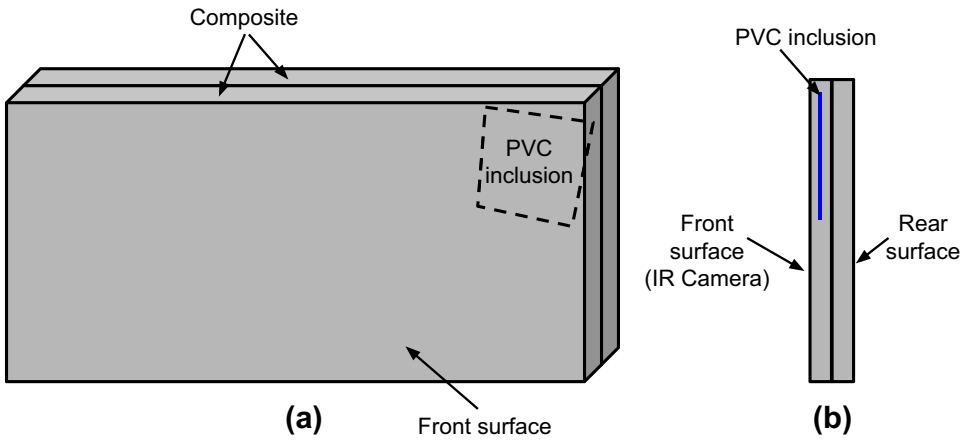


Fig. 5 Schematic drawing of composite material geometry and defect: **a** front surface and **b** side view

and positioned as shown in Fig. 3a. Note that the particular symmetry of the heater-composite assembly built in scenario 1 not only allow the numerical modeling to be simplified, but also it represents the best practice for building the experimental apparatus used for thermal property estimation of solid materials in case of the plane source method is used [31, 32]. Indeed, the analysis here reported can also be considered preliminary to the design of the experiment aimed at estimating the thermal properties of the composite material. In scenario 2, two heaters with the same dimensions were inserted into the rear surface and positioned as shown in Fig. 3b; it is observed that in this scenario there is a small region in common between the heater and the defect, but there is no contact between the two. Scenario 3 shown in Fig. 3c is the combination of scenarios 1 and 2, i.e., there is the central heater between the composites and two heaters on the rear surface. In scenarios 1, 2, and 3, the resistances of 20.92 Ω were powered by a voltage of 4 V, generating power in each heater of 0.76 W. In scenario 4, a heat source of 400.00 W heating power with dimensions equal to 120.00, 70.00, and 2.00 mm was placed 37.00 mm away from the rear surface, as shown in Fig. 3d. It is worth noting that in each scenario analyzed, a symmetric heating is applied to the sample to localize the inclusion without thermally stimulate all regions of the composite. This is a key point of the present work.

The heat transfer in the composite material and the PVC inclusion that occurs during experiments in different scenarios can be summarized by

$$k_{\mathrm{i}}\nabla^2 T = \rho_{\mathrm{i}} c_{\mathrm{i}} \frac{\partial T}{\partial t} \tag{1}$$

where i represents the layers of the sample, composite (i=1), pvc (i=2). The k, c, and ρ are, respectively, thermal conductivity, specific heat, and density of the materials.

When the existing heat source between the composites is used, heat transfer occurs in the heater with internal energy generation, which can be characterized by

$$k_{\mathrm{h}}\nabla^2 T + g = \rho_{\mathrm{h}} c_{\mathrm{h}} \frac{\partial T}{\partial t} \tag{2}$$

where k_{h}, c_{h}, and ρ_{h} are, respectively, thermal conductivity, specific heat, and density of the polyamide heater. The volumetric heat source of polyamide heater is defined as g.

For scenarios where heaters are used on the rear surface (scenarios 2, 3 and 4), partial heat flux in the contour is considered. All other surfaces are exposed to the convection boundary condition with ambient air in the laboratory. Table 1 shows the thermophysical properties considered for each material composing the sample and used in the experiment.

Note that in Table 1 the density value for the ER-GF composite was derived through the density and the volume fractions of fiber and matrix. In particular, the volume fractions of the Cytec 919 composite were inferred from technical data sheet (40% matrix and 60% fiber). Also, the density of the type "E" glass fiber (ρ_{f} =2600 kg m^{-3}) was taken from [37], while the density of the epoxy resin (ρ_{m} = 1112 kg m^{-3}) was calculated as an average of the data related to four different epoxy resins listed in [35]. Once the density of the composite (ρ_{c}) was obtained, its specific heat capacity (c_{c}) was determined using the mass fractions and the specific heat capacity of fiber (c_{f}) and matrix (c_{m}) as shown below [38].

$$c_{\mathrm{c}} = M_{\%,\mathrm{f}} c_{\mathrm{f}} + M_{\%,\mathrm{m}} c_{\mathrm{m}} = \left(\frac{\rho_{\mathrm{f}}}{\rho_{\mathrm{c}}} V_{\%,\mathrm{f}}\right) c_{\mathrm{f}} + \left(\frac{\rho_{\mathrm{m}}}{\rho_{\mathrm{m}}} V_{\%,\mathrm{m}}\right) c_{\mathrm{m}} \tag{3}$$

where the mass fractions $M_{\%,\mathrm{f}}$ and $M_{\%,\mathrm{m}}$ can be easily calculated by multiplying the volume fractions $V_{\%,\mathrm{f}}$ and $V_{\%,\mathrm{m}}$ by $(\rho_{\mathrm{f}}/\rho_{\mathrm{c}})$ and $(\rho_{\mathrm{m}}/\rho_{\mathrm{c}})$, respectively. Additionally, the

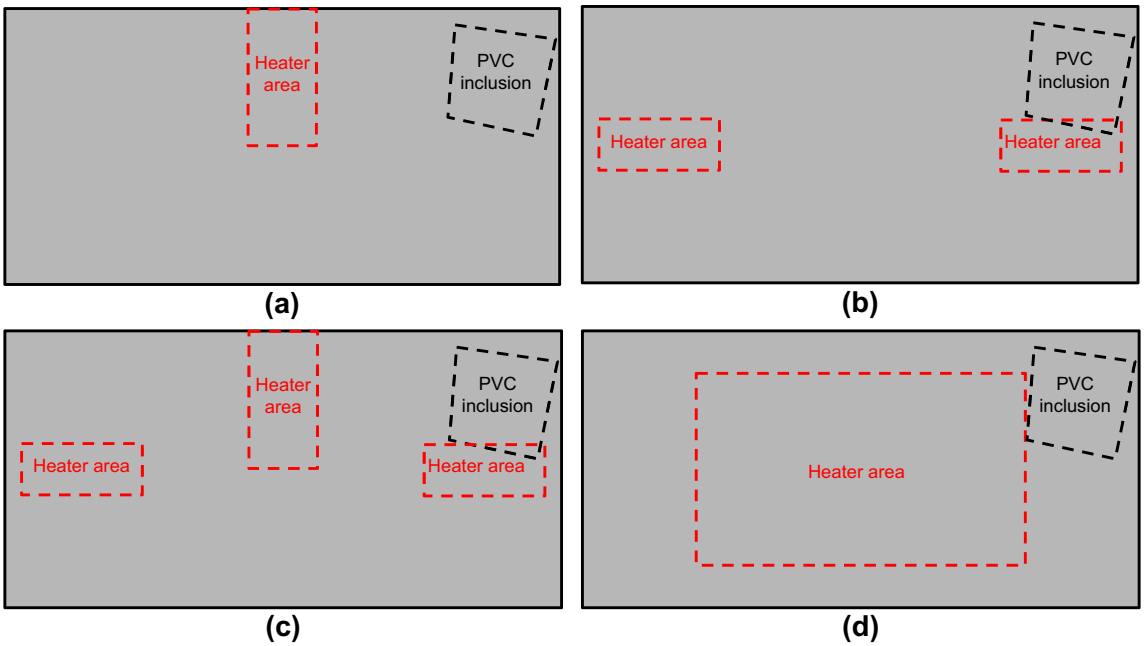


Fig. 6 Four different scenarios for sample heating: **a** scenario 1, **b** scenario 2, **c** scenario 3 and **d** scenario 4

Table 1 Thermophysical properties of the materials

Material	Thermal conductivity/W m^{-1} K^{-1}	Density/ kg m^{-3}	Specific heat/ kJ kg^{-1} K^{-1}
ER-GF Composite	0.34 [33]	2005.00	0.85
PVC-Inclusion	0.19 [34, 35]	1380.00 [36]	1.06 [36]
Polyimide-Heaters	0.29 [37]	1470.00 [37]	1.13 [37]

specific heat of fiber (c_f = 720 J kg^{-1} K^{-1}) and matrix (c_m = 1290 J kg^{-1} K^{-1}) was obtained again from [35] and [37], respectively.

Numerical simulations were performed using the commercial software COMSOL® to solve the heat transfer problem using the same boundary conditions as the experiments [39]. Initially, the transient problem was solved during the sample heating phase, and then, the transient analysis was simulated for the cooling period. Additionally, the PVC inclusion was modeled numerically without considering the thermal contact resistance with the composite, i.e., only the thermal properties of the materials were characterized as different. Figure 7 shows the numerical mesh composed of 25,479 tetrahedral elements that was considered ideal after a mesh convergence study. The detail of the mesh refinement in the region of the inclusion

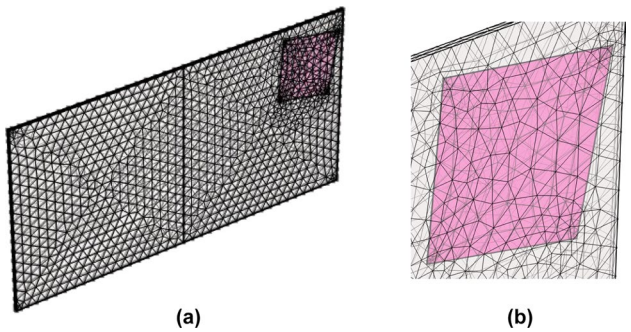


Fig. 7 Mesh used in numerical simulations: **a** overview and **b** details on the composite/inclusion interface

can be observed in Fig. 7b, where a greater quantity of elements was necessary.

Results and discussion

Experimental results

The first experiment refers to the use of scenario 1 where only a single heater was used to try to detect the defect using active thermography (Fig. 3a). A heating time of 360 s was used followed by 344 s of natural convection cooling at the laboratory ambient temperature of 297 K. The acquisition rate was 1 s, totaling 704 images acquired during the experiment. Figure 8 shows the thermographic image at the

final stage of heating, where the central region can be seen with a maximum temperature of approximately 323 K due to the presence of the heater. No difference can be seen in the image between the region with the defect and the surrounding area. At all other times analyzed, it was also not possible to observe any difference in the thermal images that would characterize the presence of a defect in the sample. Indeed, the low thermal conductivity of the composite material (see Table 1) does not allow the heat to be easily diffused throughout the sample. And the distance between the heater and the defect proved to be large enough to render the detection of the inclusion impossible.

For scenario 2, the sample was heated for 120 s and the cooling time was 300 s. Figure 9 shows a thermographic image obtained at the end of heating using the heating configuration of scenario 2 (Fig. 3b). A symmetrical heating can be observed in the image, and the maximum temperature obtained was approximately 313 K. However, no significant thermal changes that would characterize the defect were observed.

As the defect inserted in the sample proved to be difficult to detect for the chosen heating method, the normalized excess temperature was evaluated, i.e., the temperature at each point in the image was subtracted by the ambient temperature (T_∞). The result is divided by the maximum existing excess temperature, as shown in Eq. 4.

$$\theta_n = \frac{T - T_\infty}{\max(T - T_\infty)} \tag{4}$$

Figure 10 shows the normalized thermographic images with only the sample surface selected for scenario 2 at times 0, 60, 120, 180, 240, and 420 s. At time 0 s, an almost uniform distribution on the composite surface can be observed. During heating, Fig. 6b and c is unable to clearly reveal the

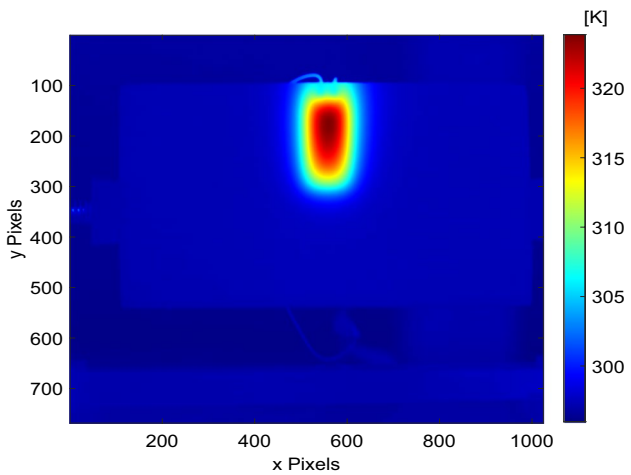


Fig. 8 Thermal image inherent to scenario 1 at 344 s

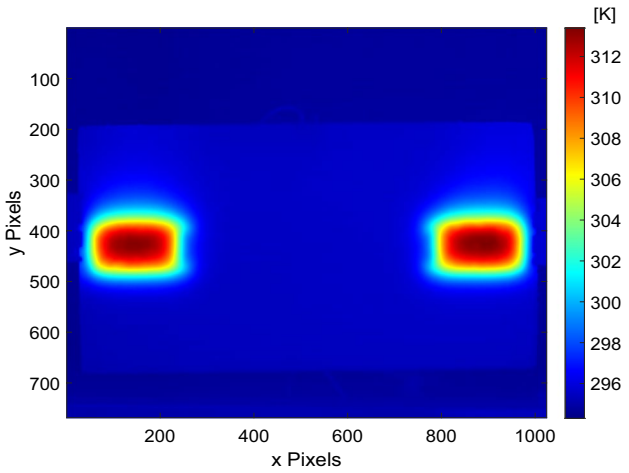


Fig. 9 Thermal image inherent to scenario 2 at the end of heating [K]

presence of the defect. During the cooling phase, mainly at 420 s, the temperature of the defect area (right side) was higher compared to the left side.

Figure 11 shows three lines in the normalized thermographic image that were created to analyze the temperature curves on the sample surface. Line 1 intersects the defect region, line 2 covers the two heaters, and line 3 does not intersect the defect and the heat source. The justification for analyzing the temperature distribution from these lines stems from the low sensitivity of the problem, thus necessitating a more specific verification to ascertain whether there are more pronounced asymmetries between the side of the component with and without defect.

Figure 12 shows the three normalized excess temperature lines for six different times. At the time of 60 s during heating, a non-symmetrical behavior in lines 1 and 3 can be observed, as shown in Fig. 12b. The temperature curve in line 2 at 120 s (Fig. 12c), the end of heating, shows symmetry between the sides of the sample, thus showing that equal heating occurred in both heaters during the experiment. Line 1 showed that the right side, the defect region, had a lower temperature gain than the non-defective side during heating and part of the cooling; this is due to the low conductivity of the material. The increase in thermal resistance makes heat transfer difficult, resulting in a lower temperature in this region. In line 3, the opposite is observed, that is, there was a greater temperature gain on the right side compared to the left. Therefore, part of the amount of heat that should have been transferred upwards (where the PVC was) went downwards (less thermal resistance), causing more heat to accumulate in relation to the left side. At the end of heating, t = 120 s, the right side of line 1 showed 20% less increase in temperature compared to the left side; in line 3, there was 10% more increase in temperature. At the end of cooling, t = 420 s, the defect region had 10%, 20%, and 25% higher

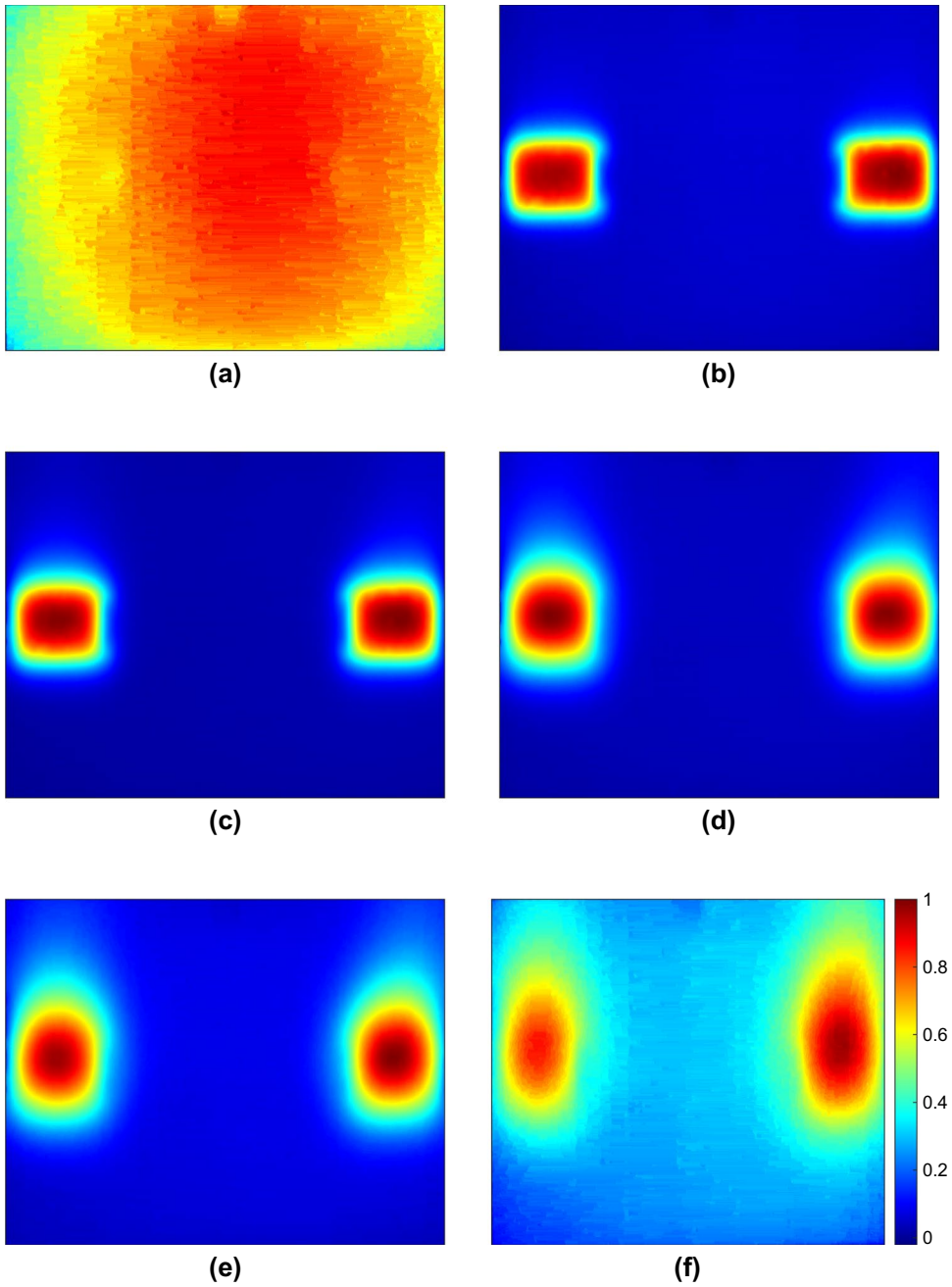


Fig. 10 Thermal images of excess temperature normalized for scenario 2: **a** 0 s, **b** 60 s, **c** 120 s, **d** 180, **e** 240 s, and **f** 420 s

temperatures compared to the non-defect side for lines 1, 2, and 3, respectively. Thus, scenario 2 was able to identify the presence of PVC inclusion due to the non-symmetrical thermal behaviors observed in the temperature gain lines.

Figure 13 shows the result of the experiment using scenario 3 (Fig. 3c), which had the same heating and cooling time as scenarios 1 and 2. The thermographic images obtained presented results similar to previous scenarios. The temperature curves analyzed did not present different results in relation to scenario 2. Therefore, it was not necessary to present further results for this scenario. The advantage of this third configuration is having an additional heater, which can help locate more defects due to the increased chances of the heat source being closer to a PVC inclusion.

For what regards the configuration of the last scenario analyzed (see Figs. 3d), Fig. 14 shows the thermographic images for the final heating time. In particular, Fig. 14a shows the general image of the experiment, and Fig. 14b shows only the composite with three lines created to analyze the temperature curves. The region on the right side heated more compared to the left side. This must have occurred because the PVC-inclusion increased the thermal resistance on the right side of the sample, resulting in

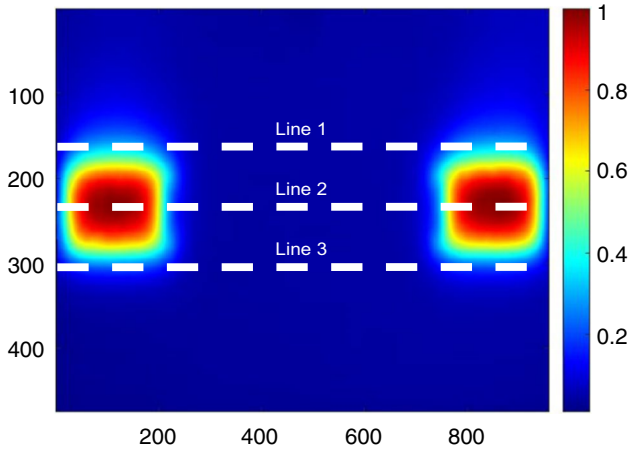


Fig. 11 Cut lines in the normalized thermographic image

the accumulation of heat in the region between the center of the composite and the defect.

Figure 15 shows the excess temperature curves obtained from lines 1, 2, and 3 shown in Fig. 14b. Lines 2 and 3, which do not pass through the defect, showed thermal symmetry between the left and right sides for all times analyzed. The times of 60, 120, and 180 s showed a significant asymmetry between the two sides of the surface for line 1. Halfway through the heating time, 60 s, a 20% greater temperature accumulation was observed on the right side (between the composite center and the PVC-inclusion). For times of 120 and 180 s, the asymmetry between temperatures decreased to 15 and 10%, respectively. During the remainder of the cooling time, no significant thermal asymmetries were observed, probably

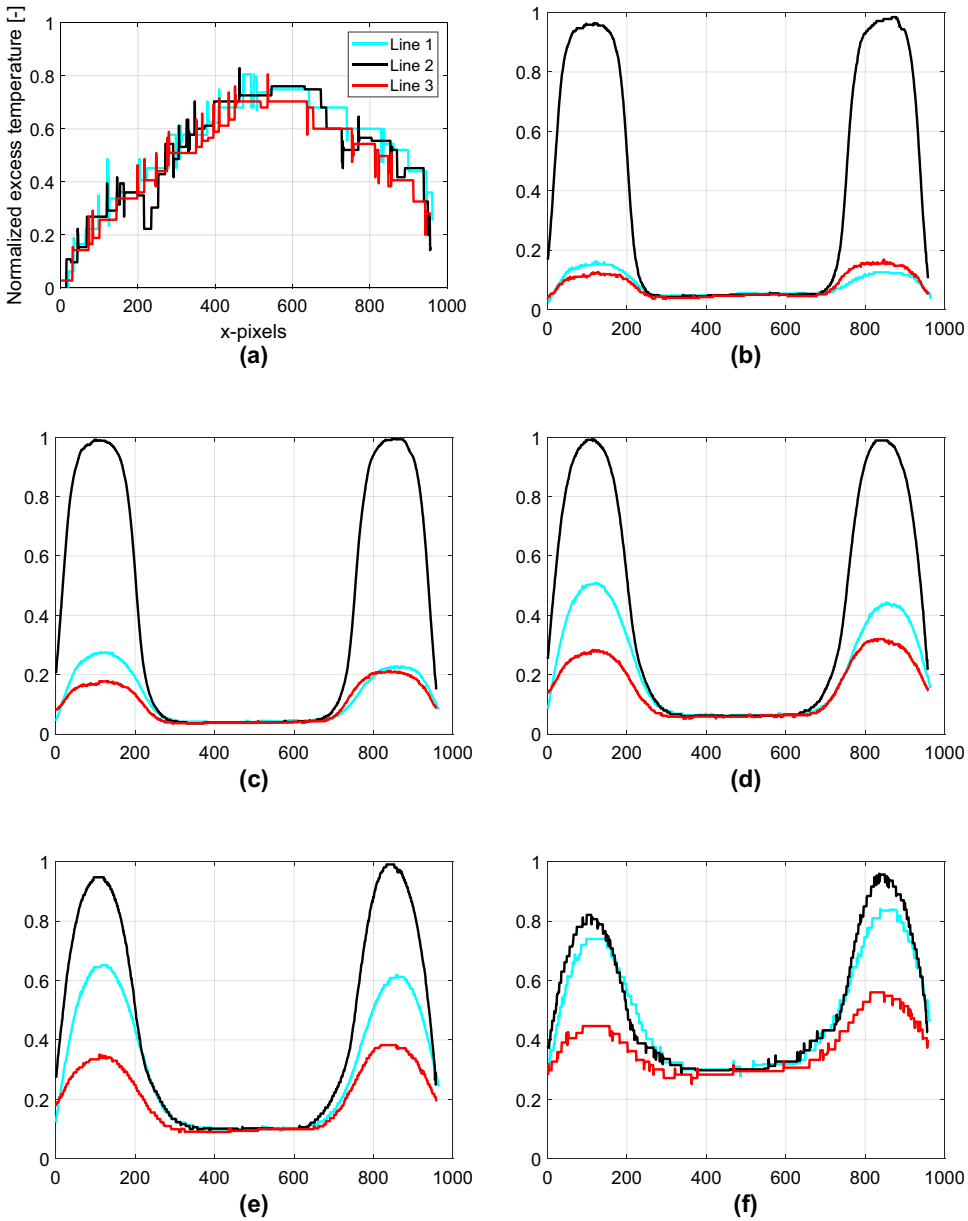


Fig. 12 Normalized excess temperature lines for scenario 2: **a** 0 s, **b** 60 s, **c** 120 s, **d** 180, **e** 240 s, and **f** 420 s

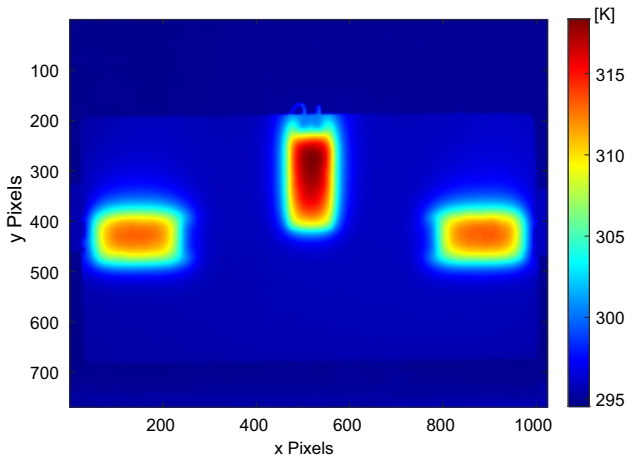


Fig. 13 Thermographic images for scenario 3 at the end of heating

due to the heating method that was non-contact with the sample, resulting in more uniform heat dissipation in the composite. Therefore, scenario 4 proved to be capable of capturing the presence of PVC inclusion from active infrared thermography. This method has an advantage over others due to the larger heating area reached in the sample, being able to detect defects in different locations using the same experiment.

Numerical results

Numerical analyses were performed using COMSOL® software. From experimental scenario 2, two different configurations were numerically simulated. Figure 16a shows the front view with two heaters arranged in the same way as in the experiments—scenario 2a. Alternatively, in Fig. 16b, the heaters were placed to overlap the defect—scenario 2b. Figure 16 includes a center line that divides sides A and B of the analyzed surface. All parameters and properties set in the simulation were the same as in the experiments, with the natural convection coefficient considered equal to 10 W m^{-2} K^{-1}, characterizing the ambient air inside the laboratory.

Initially, a model validation study was carried out based on scenario 2a, comparing the results on the frontal surface at the final heating instant (120 s) of the experiment (Fig. 17a) and numerical simulation (Fig. 17b). The behavior of the temperature distributions are similar; however, a difference was observed among the maximum temperatures obtained, that in the experiment was 313 K and in the numerical simulation was 315 K. This difference may be due to the heat losses that occur in the experiment due to the thermal contact resistance existing between the heater and the composite, and also between the layers of the sample. A horizontal cut line was created on the surface center to analyze the temperature curves and provides a better comparison among numerical and experimental results.

Figure 18a shows the experimental and numerical temperature distributions on the dotted white line drawn in Fig. 17, where temperature differences exist mainly in the heater region. Figure 18b shows the relative error between the experimental and numerical temperatures, with the maximum value of 4 %, thus validating the numerical model developed in COMSOL®.

Subtracting the images from sides B - A (Fig. 16a), Fig. 19a shows the thermal contrast of this scenario, where regions of positive and negative thermal contrasts were observed. A contrast of 0.3 K was obtained at the interface region between the heater and the PVC inclusion, that is, side B heated more than side A due to the existence of increased thermal resistance in this location. A thermal contrast of −0.1 K was obtained in the defect region, because the heat could not be transferred with the same efficiency on side B compared to side A. From the simulated results for scenario 2a, it was possible to obtain quantitative markers that indicate the presence of a defect in the composite. However, low thermal contrast values make it difficult to obtain the same results from the experiments.

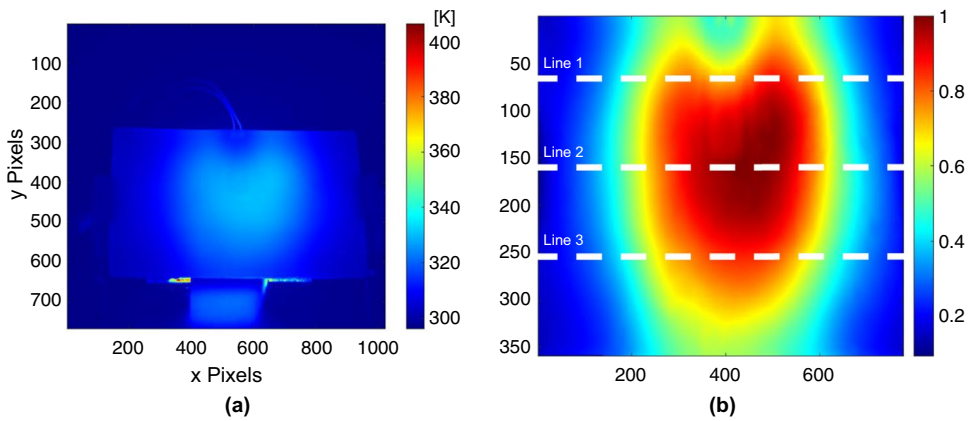


Fig. 14 Thermographic images for scenario 4 at the end of heating: **a** temperature distribution [K] and **b** normalized excess temperature distribution [-]

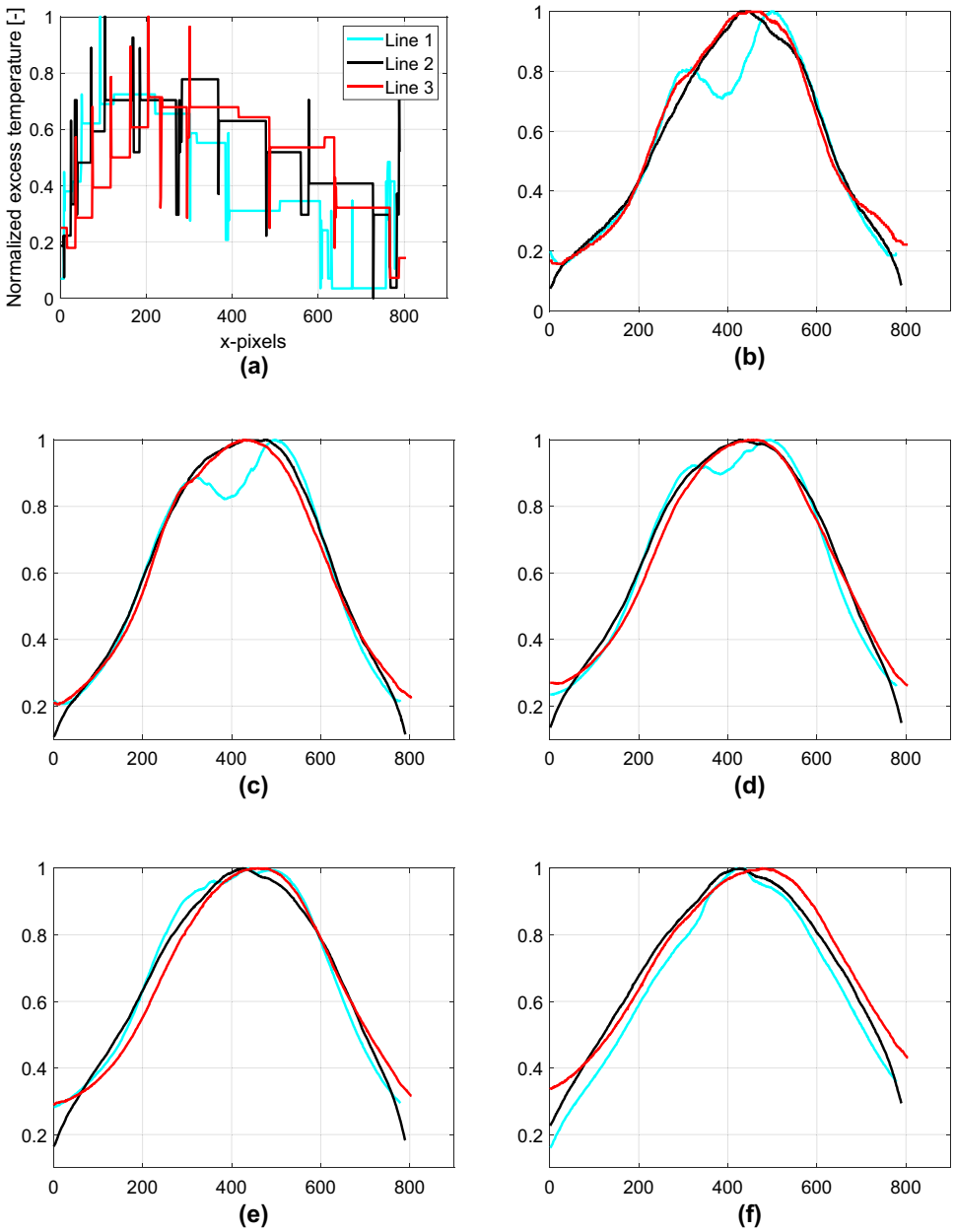


Fig. 15 Normalized excess temperature lines for scenario 4: **a** 0 s, **b** 60 s, **c** 120 s, **d** 180, **e** 240 s, and **f** 420 s

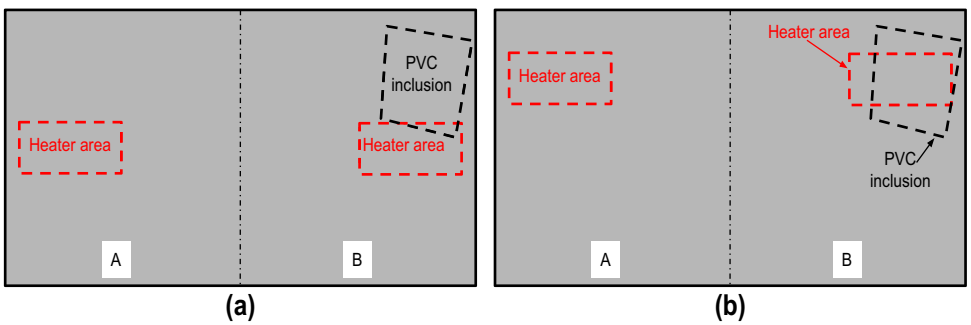


Fig. 16 Front view of numerical model: **a** scenario 2a and **b** scenario 2b

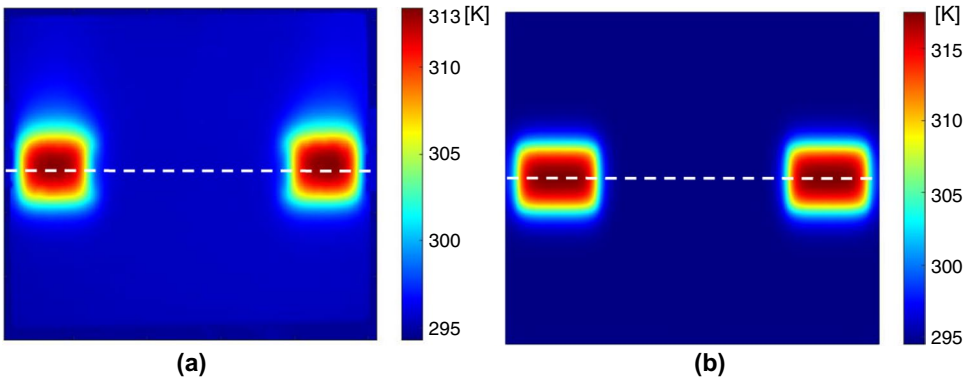


Fig. 17 Thermal image at the final instant of heating (120 s): **a** experiment and **b** numerical simulation

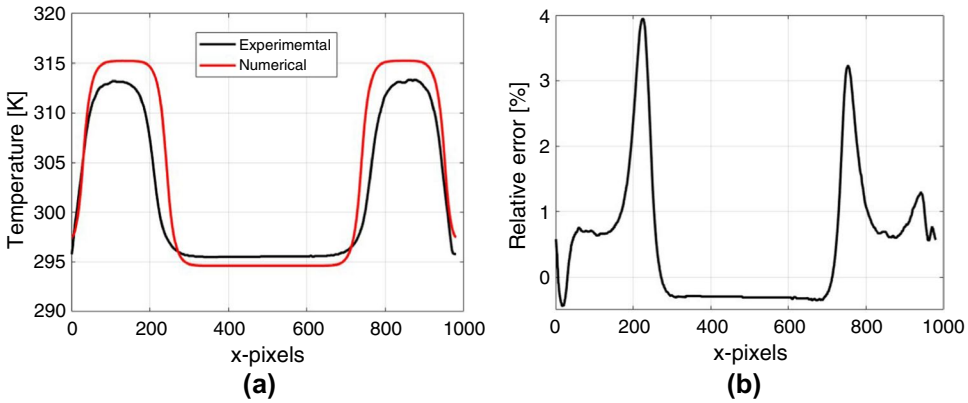


Fig. 18 Error between experimental and numerical temperatures: **a** absolute error and **b** relative error

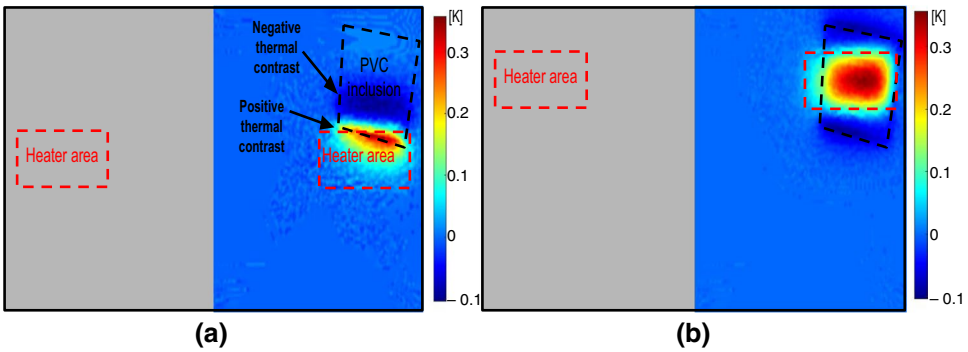


Fig. 19 Numerical thermal contrast at the end of heating (t = 120 s): **a** scenario 2a and b scenario 2b

Table 2 Percentage of thermal asymmetry from the normalized excess temperature in experiments

Scenarios	Thermal asymmetry/%
1	0
2	25
3	25
4	20

Subtracting the images from sides B - A (Fig. 16b), Fig. 19b shows the thermal contrast for the simulation in scenario 2b. In this case, a positive thermal contrast of 0.3 K in the heater center, and surrounding regions with negative thermal contrasts of −0.1 K, resulting in obtaining a clear image of the defect. Therefore, this last scenario was ideal for detecting the PVC inclusion inside the composite material. However, this last scenario would require to thermally stimulate different regions of the composite as it does not foresee a symmetric heating of the sample.

Results summary

Table 2 shows a summary of the thermal asymmetry obtained from the experimental results. In percentage terms, comparing the right and left sides of the composite sample, scenarios 1, 2, 3, and 4 showed differences in normalized temperature excesses of 0, 25, 25, and 20 %. On the one hand, the simulated thermal images showed useful markers

to identify PVC inclusion; on the other hand, the thermal asymmetries reinforce the numerical analyses thanks to the normalized excess of temperature strategy.

Therefore, the main advantages that can be highlighted in the use of localized heating scenarios when compared with flash or long pulsed thermography methods, such as flash or long pulsed thermography, are: (i) The heated area can be controlled more precisely, allowing specific areas to be selected and better control local temperature and heat distribution; (ii) Reduction in external interference is achieved, as the influence of environmental variations due to air currents or changes in ambient temperature would be reduced, resulting in more consistent and reliable images; (iii) Localized heating may be more suitable for irregular or curved surfaces, as it would guarantee a more uniform distribution of the applied heat.

However, localized heating has limitations and challenges, such as the need to prepare the experimental apparatus to ensure good contact between the heater and the sample. Another disadvantage would be the inspection time, due to the need to change the heater positions to identify the defect in the blade structure.

The applicability of the proposed method in terms of technology transfer could be foreseen in case of integration of the test pieces with a robot devoted to change recursively the position of the heaters.

Conclusions

In this active thermography experimental study, four different scenarios were evaluated to identify a defect in composite material structures of turbine blades. The results obtained provided a comprehensive view of the capabilities and limitations of each experimental setup. Scenario 1 did not show sensitivity for detecting the defect due to the significant distance between the heat source and the PVC inclusion. As the composite material has low thermal conductivity, the heating method chosen in this work requires the heat source to be close to the defect to be able to help detect its thermal signature.

Scenario 2 with two heaters was able to show asymmetries between the regions with and without defects, making it possible to use the method to track this type of failure. Scenario 3 presented thermal responses similar to scenario 2 to verify the defect in the composite material. Scenario 4, which used a larger heater in the central region, proved to be effective in characterizing the defect and may be more appropriate for a greater variety of anomaly possibilities due to its greater capacity to heat the composite, also increasing the possibility of reducing the distance between the heat source and the defect. The quantitative results when comparing the regions with and without defects on the surface of the composite sample showed differences in normalized temperature excesses of 0, 25, 25 and 20% for scenarios 1, 2, 3 and 4, respectively. Numerical analysis showed that if the heater and inclusion are overlapping, the defect reconstruction can be achieved with greater accuracy, provided that all the regions of the composite are thermally stimulated.

Based on the analyses carried out, it is possible to conclude that the appropriate heating depends on the specific characteristics of the sample and the type of defect to be identified. The applied heating needs to guarantee that the heat will be able to reach the still unknown defect; therefore, multiple heaters or a large heater may be the best strategy. The work, explained in a didactic way, should be considered of interest for university students passionate of infrared thermography. The work, indeed, leaves open the doors for more accurate quantitative evaluations of the results already found.

Acknowledgements This study was financed in part by the National Council for Scientific and Technological Development (CNPq) - Finance Codes 407.140/2021-2 and 312.530/2023-4. The authors would like to thank Prof. Francesco de Paulis (University of L'Aquila, Italy) for the fundamental help provided in building the experimental setup.

Author contributions All authors contributed to the study. SS, GDA, and HF contributed to conceptualization. AF, GDA and SS contributed to data curation and investigation. SP and SS contributed to funding acquisition and sample preparation. AF, SS and HF contributed to methodology. AF contributed to software. AF, GDA, SP, SS and HF contributed to visualization. AF, GDA, SS and HF contributed to writing review, editing, and original draft. SS and HF contributed to supervision. All authors read and approved the final manuscript.

Data availability Data supporting this study are openly available from "Numerical simulation data in COMSOL® for the two-heater scenario," Mendeley Data, V1, doi: 10.17632/9t3855jpyd.1

Open Access This article is licensed under a Creative Commons Attribution 4.0 International License, which permits use, sharing, adaptation, distribution and reproduction in any medium or format, as long as you give appropriate credit to the original author(s) and the source, provide a link to the Creative Commons licence, and indicate if changes were made. The images or other third party material in this article are included in the article's Creative Commons licence, unless indicated otherwise in a credit line to the material. If material is not included in the article's Creative Commons licence and your intended use is not permitted by statutory regulation or exceeds the permitted use, you will need to obtain permission directly from the copyright holder. To view a copy of this licence, visit http://creativecommons.org/licenses/by/4.0/.

References

1. Sanati H, Wood D, Sun Q. Condition monitoring of wind turbine blades using active and passive thermography. Appl Sci. 2018;8(10):2004. https://doi.org/10.3390/app8102004.
2. Zhang D, Zhan C, Chen L, Wang Y, Li G. Review of unmanned aerial vehicle infrared thermography (uav-irt) applications in

building thermal performance: towards the thermal performance evaluation of building envelope. Quant InfraRed Thermogr J. 2024. https://doi.org/10.1080/17686733.2024.2356913.
3. Lian J, Cai O, Dong X, Jiang Q, Zhao Y. Health monitoring and safety evaluation of the offshore wind turbine structure: a review and discussion of future development. Sustainability. 2019;11(2):494. https://doi.org/10.3390/su11020494.
4. Civera M, Surace C. Non-destructive techniques for the condition and structural health monitoring of wind turbines: a literature review of the last 20 years. Sensors. 2022;22(4):1627. https://doi.org/10.3390/s22041627.
5. Badihi H, Zhang Y, Jiang B, Pillay P, Rakheja S. A comprehensive review on signal-based and model-based condition monitoring of wind turbines: fault diagnosis and lifetime prognosis. Proceed IEEE. 2022;110(6):754–806. https://doi.org/10.1109/JPROC.2022.3171691.
6. Kaewniam P, Cao M, Alkayem NF, Li D, Manoach E. Recent advances in damage detection of wind turbine blades: a state-of-the-art review. Renew Sustain Energy Rev. 2022;167: 112723. https://doi.org/10.1016/j.rser.2022.112723.
7. Wu Z, Tao N, Zhang C, Sun J-g. Prediction of defect depth in gfrp composite by square-heating thermography. Infrared Phys Technol. 2023;130:104627. https://doi.org/10.1016/j.infrared.2023.104627.
8. Müller JP, Dell'Avvocato G, Krankenhagen R. Assessing overload-induced delaminations in glass fiber reinforced polymers by its geometry and thermal resistance. NDT E Int. 2020;116: 102309. https://doi.org/10.1016/j.ndteint.2020.102309.
9. Salazar A, Mendioroz A. Sizing the depth and width of ideal delaminations using modulated photothermal radiometry. J Appl Phys. 2022. https://doi.org/10.1063/5.0085178.
10. Ishizaki T, Nagano H. Microscale mapping of thermal contact resistance using lock-in thermography. Int J Therm Sci. 2023;193: 108475. https://doi.org/10.1016/j.ijthermalsci.2023.108475.
11. Salazar A, Sagarduy-Marcos D, Rodríguez-Aseguinolaza J, Mendioroz A, Celorrio R. Characterization of semi-infinite delaminations using lock-in thermography: Theory and numerical experiments. NDT E Int. 2023;138: 102883. https://doi.org/10.1016/j.ndteint.2023.102883.
12. Pontello A. Thermography for nondestructive testing of fuel filtration equipment and other applications. In: Materials Evaluation, 1972; vol. 30, p. 35. AMER SOC NON-DESTRUCTIVE TEST 1711 Arlingate Lane Po Box 28518, Colombus, OH 43228-0518:
13. Galleguillos C, Zorrilla A, Jimenez A, Diaz L, Montiano Á, Barroso M, Viguria A, Lasagni F. Thermographic non-destructive inspection of wind turbine blades using unmanned aerial systems. Plast , Rubber Compos. 2015;44(3):98–103. https://doi.org/10.1179/1743289815Y.0000000003.
14. Worzewski T, Krankenhagen R, Doroshtnasir M, Röllig M, Maierhofer C, Steinfurth H. Thermographic inspection of a wind turbine rotor blade segment utilizing natural conditions as excitation source, part i: Solar excitation for detecting deep structures in gfrp. Infrared Phys Technol. 2016;76:756–66. https://doi.org/10.1016/j.infrared.2016.04.011.
15. Worzewski T, Krankenhagen R, Doroshtnasir M. Thermographic inspection of wind turbine rotor blade segment utilizing natural conditions as excitation source, part ii: The effect of climatic conditions on thermographic inspections-a long term outdoor experiment. Infrared Phys Technol. 2016;76:767–76. https://doi.org/10.1016/j.infrared.2016.04.012.
16. Almond DP, Angioni SL, Pickering SG. Long pulse excitation thermographic non-destructive evaluation. NDT E Int. 2017;87:7–14. https://doi.org/10.1016/j.ndteint.2017.01.003.
17. Jensen F, Jerg JF, Sorg M, Fischer A. Active thermography for the interpretation and detection of rain erosion damage evolution on gfrp airfoils. NDT E Int. 2023;135: 102778. https://doi.org/10.1016/j.ndteint.2022.102778.
18. Krishnapillai M, Jones R, Marshall IH, Bannister M, Rajic N. Ndte using pulse thermography: Numerical modeling of composite subsurface defects. Compos Struct. 2006;75(1–4):241–9. https://doi.org/10.1016/j.compstruct.2006.04.079.
19. Sfarra S, Tejedor B, Perilli S, Almeida RM, Barreira E. Evaluating the freeze-thaw phenomenon in sandwich-structured composites via numerical simulations and infrared thermography. J Therm Anal Calorim. 2021;145(6):3105–23. https://doi.org/10.1007/s10973-020-09985-1.
20. Colom M, Rodríguez-Aseguinolaza J, Mendioroz A, Salazar A. Sizing the depth and width of narrow cracks in real parts by laser-spot lock-in thermography. Materials. 2021;14(19):5644. https://doi.org/10.3390/ma14195644.
21. Rodríguez-Aseguinolaza J, Colom M, González J, Mendioroz A, Salazar A. Quantifying the width and angle of inclined cracks using laser-spot lock-in thermography. NDT E Int. 2021;122: 102494. https://doi.org/10.1016/j.ndteint.2021.102494.
22. Addante GD, Dell'Avvocato G, Bisceglia F, D'Accardi E, Palumbo D, Galietti U. Laser thermography: an investigation of test parameters on detection and quantitative assessment in a finite crack. Eng Proceed. 2023;51(1):7. https://doi.org/10.3390/engproc2023051007.
23. Notebaert A, Quinten J, Moonens M, Olmez V, Barros C, Cunha SS Jr, Demarbaix A. Numerical modelling of the heat source and the thermal response of an additively manufactured composite during an active thermographic inspection. Materials. 2023;17(1):13. https://doi.org/10.3390/ma17010013.
24. Zhao S, Zhang Cl, Wu NM, Duan YX, Li H. Infrared thermal wave nondestructive testing for rotor blades in wind turbine generators non-destructive evaluation and damage monitoring. In: International Symposium on Photoelectronic Detection and Imaging 2009: Advances in Infrared Imaging and Applications; 2009. vol. 7383; pp. 540–547. https://doi.org/10.1117/12.835123 . SPIE
25. Doroshtnasir M, Worzewski T, Krankenhagen R, Röllig M. On-site inspection of potential defects in wind turbine rotor blades with thermography. Wind energy. 2016;19(8):1407–22. https://doi.org/10.1002/we.1927.
26. Hwang S, An Y-K, Sohn H. Continuous line laser thermography for damage imaging of rotating wind turbine blades. Procedia Eng. 2017;188:225–32. https://doi.org/10.1016/j.proeng.2017.04.478.
27. Yang R, He Y, Mandelis A, Wang N, Wu X, Huang S. Induction infrared thermography and thermal-wave-radar analysis for imaging inspection and diagnosis of blade composites. IEEE Trans Indus Inform. 2018;14(12):5637–47. https://doi.org/10.1109/TII.2018.2834462.
28. Hwang S, An Y-K, Yang J, Sohn H. Remote inspection of internal delamination in wind turbine blades using continuous line laser scanning thermography. Int J Precis Eng Manuf -Green Technol. 2020;7(3):699–712. https://doi.org/10.1007/s40684-020-00192-9.
29. Sfarra S, Cicone A, Yousefi B, Perilli S, Robol L, Maldague XP. Maximizing the detection of thermal imprints in civil engineering composites via numerical and thermographic results pre-processed by a groundbreaking mathematical approach. Int J Therm Sci. 2022;177: 107553. https://doi.org/10.1016/j.ijthermalsci.2022.107553.
30. Figueiredo A, D'Alessandro G, Perilli S, Sfarra S, Fernandes H. Numerical and experimental analysis for flaw detection in composite structures of wind turbine blades using active infrared thermography. In: 4th Asian Quantitative Infrared Thermography Conference. 2023. https://doi.org/10.21611/qirt.2023.08.
31. D'Alessandro G, de Monte F. On the optimum experiment and heating times when estimating thermal properties through the

plane source method. Heat Transf Eng. 2021;43(3–5):257–69. https://doi.org/10.1080/01457632.2021.1874655.
32. D'Alessandro G, de Monte F, Gasparin S, Berger J. Comparison of uniform and piecewise-uniform heatings when estimating thermal properties of high-conductivity materials. Int J Heat Mass Transf. 2023;202: 123666. https://doi.org/10.1016/j.ijheatmasstransfer.2022.123666.
33. Assael M, Antoniadis K, Tzetzis D. The use of the transient hot-wire technique for measurement of the thermal conductivity of an epoxy-resin reinforced with glass fibres and/or carbon multi-walled nanotubes. Compos Sci Technol. 2008;68(15–16):3178–83. https://doi.org/10.1016/j.compscitech.2008.07.019.
34. Mathur V, Arya PK, Sharma K. Estimation of activation energy of phase transition of PVC through thermal conductivity and viscosity analysis. Mater Today: Proceed. 2021;38:1237–40. https://doi.org/10.1016/j.matpr.2020.07.553.
35. de Carvalho G, Frollini E, Santos WND. Thermal conductivity of polymers by hot-wire method. J Appl Polym Sci. 1996;62(13):2281–5.
36. Web CR. Polymer database. http://polymerdatabase.com. Accessed: October 2022.
37. UBE Corporation. https://www.ube.com. Accessed: October 2022.
38. Zhang Y, Cameron J. Evaluation of fibre content in glass fibre epoxy composites from heat capacity data. J Reinf Plast Compos. 1992;11(8):939–48. https://doi.org/10.1177/073168449201100805.
39. Perilli S, Regi M, Sfarra S, Nardi I. Comparative analysis of heat transfer for an advanced composite material used as insulation in the building field by means of comsol multiphysics®and matlab ®computer programs. Revista Romana de Materiale/ Roman J Mater. 2016;46(2):185–95.

Publisher's Note Springer Nature remains neutral with regard to jurisdictional claims in published maps and institutional affiliations.



https://dspace.org/

Exploring the potentialities of thermal asymmetries in composite wind turbine blade structures via numerical and thermographic methods: a thermophysical perspective

Figueiredo, Alisson A. A.; D'Alessandro, G.; Perilli, Stefano; Sfarra, Stefano; Fernandes, Henrique

2025-06
Springer
https://doi.org/10.1007/s10973-024-13584-9
Figueiredo AAA, D'Alessandro G, Perilli S, et al., (2025) Exploring the potentialities of thermal asymmetries in composite wind turbine blade structures via numerical and thermographic methods: a thermophysical perspective. Journal of Thermal Analysis and Calorimetry, Volume 150, June 2025, pp. 8107-8121

Downloaded from a DSpace repository. https://dspace.org/